

Energy Level Structure of Sn³⁺ Ions

J. Scheers,^{1,2} A. Ryabtsev,³ A. Borschevsky,⁴ J. C. Berengut,⁵ K. Haris,⁶ R. Schupp,¹ D. Kurilovich,^{1,2}
F. Torretti,^{1,2} A. Bayerle,¹ E. Eliav,⁷ W. Ubachs,^{1,2} O. O. Versolato,¹ and R. Hoekstra^{1,8,*}

¹*Advanced Research Center for Nanolithography, Science Park 110, 1098 XG Amsterdam, The Netherlands*

²*Department of Physics and Astronomy, and LaserLaB, Vrije Universiteit,*

De Boelelaan 1081, 1081 HV Amsterdam, The Netherlands

³*Institute of Spectroscopy, Russian Academy of Sciences, Troitsk, Moscow, 108840 Russia*

⁴*Van Swinderen Institute, University of Groningen,
Nijenborgh 4, 9747 AG Groningen, The Netherlands*

⁵*School of Physics, University of New South Wales, Sydney 2052, Australia*

⁶*Department of Physics, Aligarh Muslim University, Aligarh, 202002, India*

⁷*School of Chemistry, Tel Aviv University, 69978 Tel Aviv, Israel*

⁸*Zernike Institute for Advanced Materials, University of Groningen,
Nijenborgh 4, 9747 AG Groningen, The Netherlands*

(Dated: July 5, 2018)

Laser-produced Sn plasma sources are used to generate extreme ultraviolet (EUV) light in state-of-the-art nanolithography. An ultraviolet and optical spectrum from a droplet-based laser-produced Sn plasma, with a spectrograph covering the range 200 - 800 nm. This spectrum contains hundreds of spectral lines from lowly charged tin ions Sn¹⁺ - Sn⁴⁺ of which a major fraction was hitherto unidentified. We present and identify a selected class of lines belonging to the quasi-one-electron, Ag-like ([Kr]4d¹⁰nl electronic configuration), Sn³⁺ ion, linking the optical lines to a specific charge state by means of a masking technique. These line identifications are made with iterative guidance from COWAN code calculations. Of the 53 lines attributed to Sn³⁺, some 20 were identified from previously known energy levels, and 33 lines are used to determine previously unknown level energies of 13 electronic configurations, i.e., 7p, (7,8)d, (5,6)f, (6-8)g, (6-8)h, (7,8)i. The consistency of the level energy determination is verified by the quantum-defect scaling procedure. The ionization limit of Sn³⁺ is confirmed and refined to 328 908.4 cm⁻¹ with an uncertainty of 2.1 cm⁻¹. The relativistic Fock space coupled cluster (FSCC) calculation of the measured level energies are generally in good agreement with experiment, but fail to reproduce the anomalous behavior of the 5d ²D and nf ²F terms. By combining the strengths of FSCC, COWAN code calculations, and configuration interaction many-body perturbation theory (CI+MBPT), this behavior is shown to arise from interactions with doubly-excited configurations.

I. INTRODUCTION

Emission of light by neutral tin atoms and lowly charged tin ions, Sn I - Sn V, is abundant in a wide variety of plasmas, ranging from laser-produced extreme-ultraviolet (EUV) light generating Sn plasma for nanolithography [1, 2], divertor plasma when using tin containing materials in future thermonuclear fusion reactors [3-5], discharge plasma between tin whiskers causing short-circuits [6], to astrophysical environments [7-15]. Spectroscopic investigations on these kinds of plasmas can help characterize plasma parameters [16-22] such as ion and electron densities and temperatures by studying the observed line strengths and their shapes. However, spectroscopic information on the relevant charge states Sn³⁺ and Sn⁴⁺, i.e., Sn IV and Sn V, is rather scarce, because of the poorly known electronic structure of these ions.

Sn³⁺, with its ground electronic configuration [Kr]4d¹⁰5s, belongs to the Ag-like isoelectronic sequence. Remarkably, only the lowest eight singly-excited 4d¹⁰nl,

the doubly-excited 4d⁹5s² and three 4d⁹5s5p levels in Sn³⁺ are tabulated in the NIST database [23]. The level energies originate from unpublished work by Shenstone [24], while wavelengths are given in another compilation by the National Bureau of Standards [25]. The assessment of energy levels by Shenstone is based on extended and revised work by Lang and others [26-29]. Since the early compilation [24] of almost 60 years ago, the only extension of the electronic energy level structure of Sn IV stems from EUV spectroscopy by Ryabtsev and coworkers [30] in which they extend the ns series from n = 8 up to n = 10 and add the 7d ²D term. A more extensive list of Sn IV lines is given in an otherwise unpublished MSc thesis [31]. In other works, beam-foil techniques have been used to determine lifetimes [32-34]. Aside of the singly-excited levels, some doubly-excited energy levels belonging to the 4d⁹5s5p configuration are identified in laser- and vacuum-spark-produced tin plasmas [30, 35-39]. Theoretical level energies and transition probabilities [40, 41] have been calculated for Ag-like ions. The narrow, inverted fine structure of the 4f ²F term in Ag-like Sn³⁺ has been addressed in detail by theory [40-44]. In spite of all these efforts, knowledge of the electronic structure of Sn IV is mostly limited to its lowest energy levels.

* r.a.hoekstra@rug.nl

To obtain the electronic structure of Sn^{3+} , we have studied its line emission in the wavelength range of 200 – 800 nm. The optical lines belonging to Sn IV are identified amongst the hundreds of optical lines stemming from a laser-produced droplet-based Sn plasma, by taking spectra as a function of laser intensity. The method to single out transitions belonging to ions in a specific charge state relies on the strongly changing ratio between line intensity and background emission from the plasma as a function of laser intensity.

We will first introduce and detail a convenient method to obtain charge-state-resolved optical spectra from a laser-produced plasma (LPP) in the following. Out of the over 350 lines observed in the visible spectral range, 53 are identified as stemming from Sn^{3+} . Out of those, 33 lines are new determinations. Thereafter, the line identification is discussed. On basis of these line identifications an extended level diagram for Sn^{3+} is constructed. The consistency of the highly-excited levels is checked by quantum-defect scalings. In the final section, Fock space coupled cluster (FSCC) and configuration interaction many-body perturbation theory (CI+MBPT) calculations are employed to explain the anomalous behavior of the $5d^2D$ and nf^2F terms.

II. EXPERIMENTAL SETUP

An overview of the experimental setup is depicted in Fig. 1. A more detailed explanation is provided in Ref. [45]. The experimental LPP source consists of a vacuum vessel (about 10^{-7} mbar) equipped with a droplet generator from which a 10 kHz stream of liquid tin microdroplets is ejected. The droplets have a diameter of about $45 \mu\text{m}$. A 10-Hz pulsed Nd:YAG laser, operating at its fundamental wavelength of 1064 nm, is used to irradiate the droplets in order to generate a plasma. The laser energy is varied without changing the beam shape by using the combination of a half-wave plate ($\lambda/2$) and a thin-film polarizer (TFP), reflecting part of the light into a beamdump (BD). The laser beam is circularly polarized by a quarter-wave plate ($\lambda/4$), hereafter the beam is focused onto the droplet. This results in a Gaussian full-width-at-half-maximum (FWHM) beam size of $115 \mu\text{m}$ at the droplet position. The laser has a 10 ns FWHM pulse length. Light reflected by the droplet falling through a helium-neon (HeNe) laser sheet is detected by a photomultiplier tube (PMT) used to trigger the laser.

The light emitted from the plasma is observed through a viewport perpendicular to the laser beam propagation and 30 degrees above the horizontal plane. A bi-convex lens images the plasma onto a quartz fiber that is used to guide the light to the spectrometer (Princeton Isoplan SCT 320). The entrance side of the fiber consists of 19 cores with a diameter of $200 \mu\text{m}$ in a hexagonal configuration, while at the exit side the cores are oriented in a linear configuration to efficiently guide light through the spectrometer slit. The spectrometer

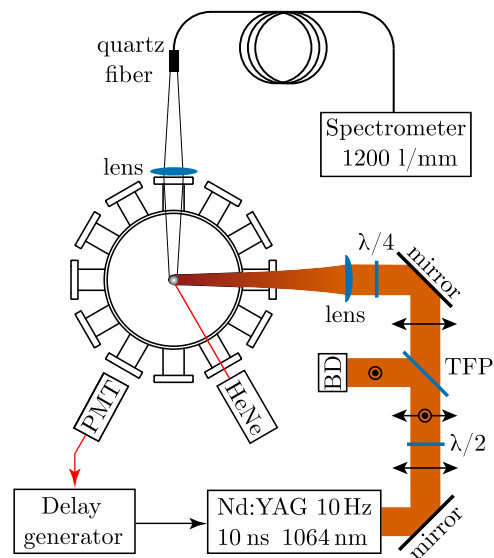


FIG. 1. Schematic top view of the main components of the LPP source from which the spectroscopic data was taken. For details see Section II.

is laid out in a Czerny-Turner configuration with a focal length of 320 mm. The grating has 1200 lines per mm and is blazed at 500 nm, leading to a significantly reduced grating diffraction efficiency below 300 nm. A CCD camera (Princeton Pixis 2KBV) optimized for the ultraviolet and visible regime recorded the diffracted light. By rotating the grating, thus changing the spectral detection range, the full spectral range from 200 to 800 nm is covered in steps of approximately 50 nm, overlapping by about 10 nm. From the shortest to the longest wavelength the linear dispersion decreases from 0.033 to 0.028 nm per pixel.

The wavelength axis is calibrated using neon-argon and mercury lamps. The FWHM line widths of the calibration lines are smaller than 0.1 nm. The total uncertainties of the mid positions of the Sn^{3+} lines are better than 0.01 nm over all observed laser energies and wavelengths. The emitted light is space- and time-integrated by summing the intensity resulting from the various fiber cores and taking an integration time of 10 s, corresponding to 100 laser shots.

Measurements are performed with, and without, edge-pass filters to distinguish second-order lines from first-order ones. This enables filtering out the second-order lines appearing at wavelengths longer than 400 nm. Additionally, closely packed lines in the ultraviolet below 300 nm can be determined in second order at a higher resolution. Weakly appearing lines in first order, due to the low grating response below 300 nm, are observed with a higher intensity in second order.

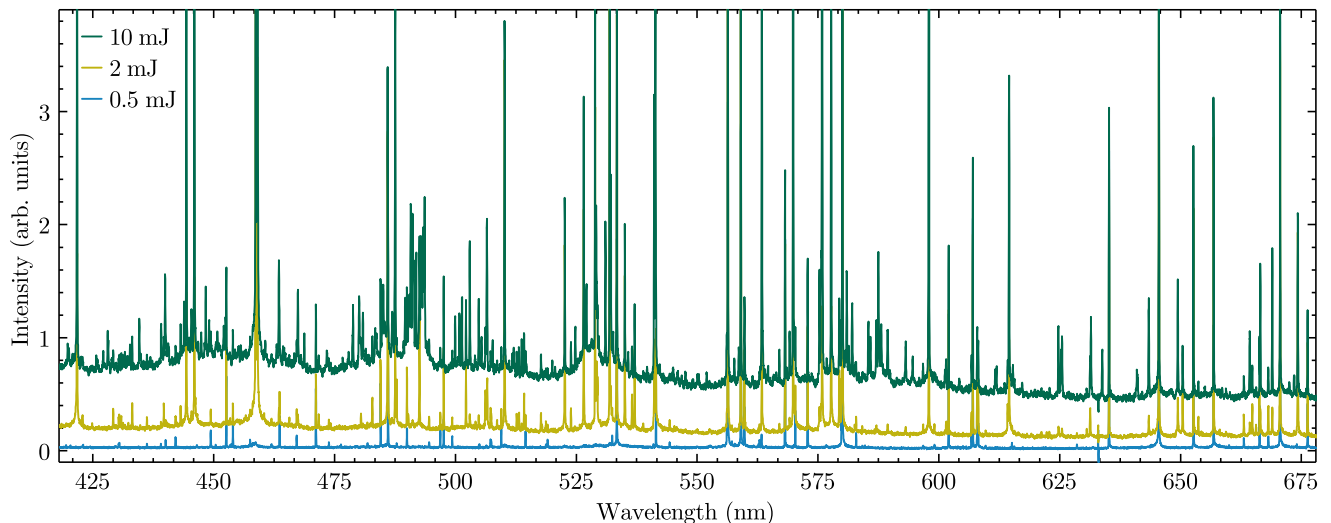


FIG. 2. Experimentally obtained Sn^{q+} spectra for laser energies of 0.5 mJ (blue, lower), 2 mJ (yellow, middle), and 10 mJ (green, upper). The observable increase in the background level is due to increased continuum emission from the plasma for higher laser energies. The spectra shown are taken without spectral filters and, thus, include second order contributions.

III. CHARGE STATE IDENTIFICATION

We performed passive spectroscopy measurements on the laser-produced tin plasma for a series of laser energies ranging from 0.5 to 370 mJ. Fig. 2 shows example measurements over a selected wavelength range for three laser energies, where it is shown that the number of lines increases with laser energy. This is a signature of an increasing number of contributing charge states to the measured spectrum. A closer inspection indicates that indeed sets of lines appear with increasing laser energy that exhibit similar changes in intensity. As will be demonstrated below, each of these sets of lines can be singled out by considering their intensities with respect to the continuum background, increasing strongly with laser energy.

To illustrate the procedure we select a well-known line of each of the charge states Sn I – Sn V . These are the $\text{Sn I } 5p^2 \ ^1S_0 - 5p 6s \ ^1P_1$ ($\lambda=452.60$ nm [46]), $\text{Sn II } 5d \ ^2D_{5/2} - 4f \ ^2F_{7/2}$ ($\lambda=580.05$ nm [47]) (the transition from the $4f \ ^2F_{5/2}$ at 579.85 nm is also visible), $\text{Sn III } 6s \ ^1S_0 - 6p \ ^1P_1$ ($\lambda=522.64$ nm [48]), $\text{Sn IV } 6s \ ^2S_{1/2} - 6p \ ^2P_{1/2}$ ($\lambda=421.73$ nm) and $\text{Sn V } 6s \ ^3D_3 - 6p \ ^3F_4$ ($\lambda=315.6$ nm, based on level energies taken from Refs. [49, 50]). The scaled intensity is defined as $I_\lambda/I_{\text{bg}} - 1$, with I_λ the line intensity and I_{bg} the (local value of the) continuum background level. For direct comparison, the scaled intensity of each individual line is normalized to its maximum value, as shown in Fig. 3. From Fig. 3, it is seen that for the lowest charge states Sn I and Sn II the normalized, scaled intensity maximizes for the lowest laser energy of 0.5 mJ, while for the highest observed charge state Sn V a laser energy of 10 mJ is optimal. Sn IV , the ion of interest here, maximizes at 2 mJ. This demonstrates that the contributions of higher

charge states to the spectrum increase with increasing laser energy. Preliminary nanosecond time-resolved spectroscopic measurements revealed that spectral line emission is mostly observed in the late-time evolution of the plasma. Traces of line broadening are observed in the time-integrated spectra presented in this work, e.g., the Sn IV line shape in the 2 mJ spectrum. Analysis of line broadening mechanisms and the time-evolution of these plasmas will be left for future work as they do not influence our line identifications and are outside the scope of this paper.

Fig. 4 quantifies the dependence of the scaled intensities for spectral lines belonging to tin ions in charge states 0, 1, 2, 3, and 4+ produced in the Sn LPP. The unique energy dependence of each charge state enables a straightforward assignment of unknown lines to specific charge states. In this way 53 lines are assigned to Sn IV .

IV. LINE IDENTIFICATION PROCEDURE

Of the 53 lines in the ultraviolet and optical spectral range attributed to Sn IV , 20 are readily identified as transitions between energy levels known from literature [24], and match well within mutual experimental uncertainties with the line positions given in Ref. [31]. These 20 lines are presented in Table I along with their connecting upper and lower energy levels.

Having identified 20 lines using known energy levels, we proceed with the identification of the other lines ascribed to Sn IV . Unique identifications of the observed lines requires an accuracy of the level energies of better than 10^{-3} , which is challenging for atomic theories. Therefore, an iterative procedure is used to identify the unknown lines. We use the COWAN code to calculate the electronic

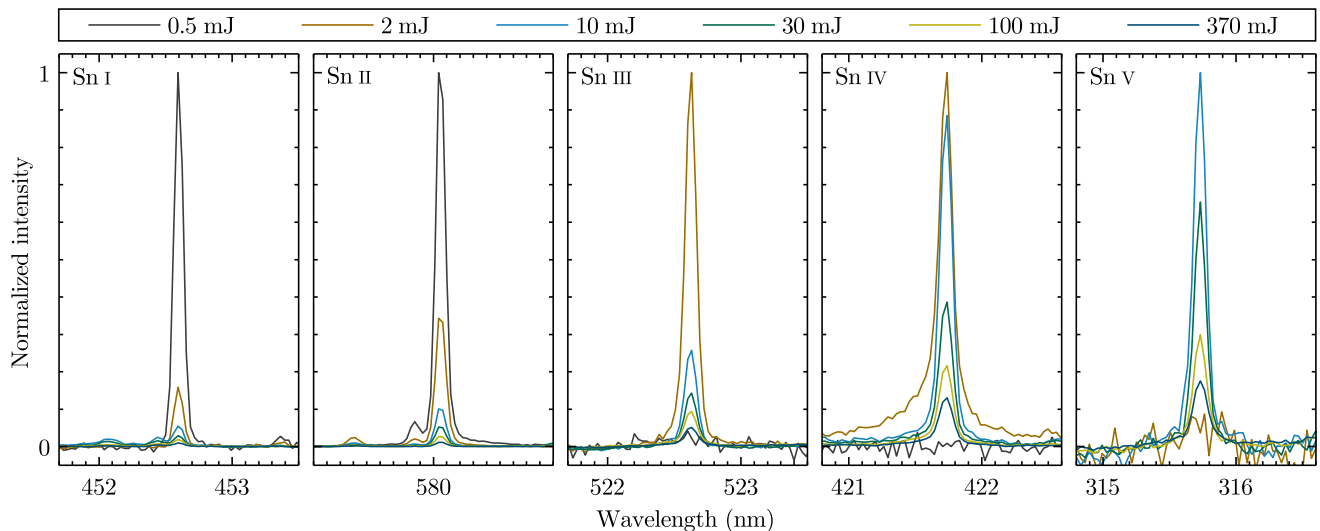


FIG. 3. Spectral intensity scaling as a function of wavelength (vacuum, in nm) for varying laser energy. Here, the intensity is normalized to their (local) continuum background level, and unity is subsequently subtracted. The laser energies depicted are 0.5 mJ (black), 2 mJ (brown), 10 mJ (light blue), 30 mJ (green), 100 mJ (yellow) and 370 mJ (dark blue). The specific transitions shown are described in the text.

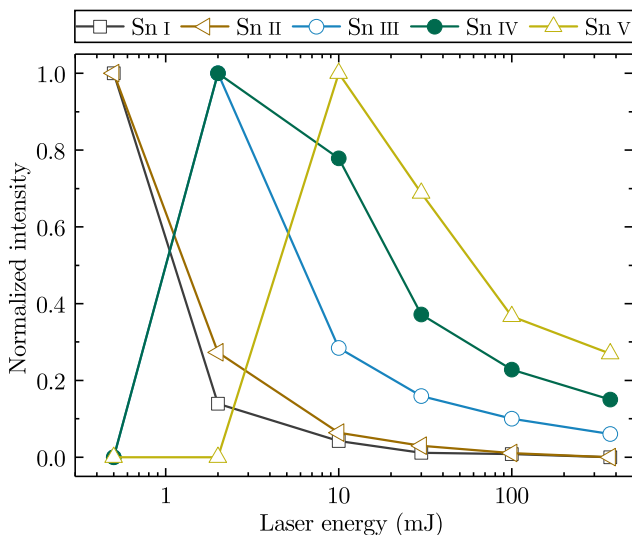


FIG. 4. Normalized scaled intensities of Sn I–Sn V lines as a function of laser energy. The same lines as presented in Fig. 3 are used. Other Sn I–Sn V lines show a similar dependence on laser energy.

structure and transitions, and adjust its parameters to match perfectly the known lines in the spectrum. In this way, energy levels just above the known ones can be obtained with sufficient accuracy to identify a next set of lines. This procedure can be repeated to identify all lines. Furthermore, quantum defect theory [51] is used to check the consistency of level energies for each l series.

A. COWAN procedure

The COWAN code [52], one of the most widely applied electronic structure codes, is used to calculate the energies of yet unestablished Sn IV levels. The COWAN code produces radial wave functions using a quasi-relativistic Hartree-Fock method. The electrostatic single configuration radial integrals F_k and G_k (Slater integrals), configuration interaction, Coulomb radial integrals and spin-orbit parameters are calculated from the obtained wavefunctions. Subsequently, level energies and intermediate coupling eigenvectors are extracted. Furthermore, values for the transition probabilities and wavelengths are obtained.

The values of the electrostatic integrals are scaled by a factor between 0.7 and 0.85 as well as the scaling of spin-orbit parameters to optimally fit the thus far understood experimental spectrum. The outcome of this parameter scaling procedure yields a useful interpretation of the experimental spectrum. This enables predictions for lines between not yet experimentally established energy levels. These predictions include their relative strength expressed as the gA factor: the Einstein coefficient A multiplied with the statistical weight g of the upper state. Due to the one-electron nature of the system, the number of allowed transitions between two terms is only three (or two if a 2S term is involved). However, we might observe only two lines since transitions between equal angular momenta have typically a small gA factor. Experimental lines that lie close to a predicted transition and have relative line strengths similar to the ones determined on basis of the aforementioned gA factors are thus assigned to a specific transition. This provides an enlarged set of levels that can be used to fine-tune the calculations in a

TABLE I. Vacuum wavelengths (in nm) of Sn IV lines between levels previously known. The wavelengths determined in this work are compared with literature values taken from an otherwise unpublished Master's thesis [31]. The upper and lower energy levels indicating the transition represent the nl one-electron orbital outside the [Kr]4d¹⁰ core configuration. The 5s² indicates the doubly-excited 4d⁹5s² configuration. The wavelengths determined in this work are averaged centroid positions of Gaussian fits in spectra taken at different laser energies. The intensity I represents the area-under-the-curve of this line in the 30 mJ spectrum. gA factors from the upper level result from analysis with the COWAN code.

λ (nm)		I (arb.un.)	gA (10 ⁸ s ⁻¹)	lower		upper	
this work	literature			nl	J	nl	J
208.23	208.224	25	130.2	4f 7/2	5g 9/2		
208.49	208.485	20	100.4	4f 5/2	5g 7/2		
222.14	222.156	289	53.8	5d 3/2	4f 5/2		
222.66	222.680	1	3.4	5d 5/2	4f 5/2		
222.96	222.980	34	68.5	5d 5/2	4f 7/2		
243.75	243.757	35	6.6	5s ² 5/2	4f 7/2		
251.47	251.466	22	6.0	6p 1/2	7s 1/2		
266.05	266.054	48	10.1	6p 3/2	7s 1/2		
270.68	270.667	154	27.5	6p 1/2	6d 3/2		
284.91	284.922	351	42.2	6p 3/2	6d 5/2		
287.64	287.633	38	4.6	6p 3/2	6d 3/2		
287.96	287.961	32	1.5	5d 3/2	6p 3/2		
288.85	288.840	219	11.2	5d 5/2	6p 3/2		
307.26	307.247	251	6.0	5d 3/2	6p 1/2		
324.71	324.700	166	1.6	5s ² 5/2	6p 3/2		
386.23	386.232	1063	9.2	6s 1/2	6p 3/2		
402.08	402.071	289	4.5	4f 7/2	6d 5/2		
403.03	403.076	30	0.2	4f 5/2	6d 5/2		
408.52	408.520	219	3.0	4f 5/2	6d 3/2		
421.73	421.735	677	3.5	6s 1/2	6p 1/2		

next step.

B. Quantum defect

The energy levels of quasi-one-electron systems approach a hydrogen-like level structure, especially for high principal and angular quantum numbers. For such systems the energy levels which are shifted towards slightly higher binding energies can be well-described by introducing the so-called quantum defect δ_l as a correction to the Bohr formula. The position of energy level E_{nl} (relative to the ionization limit) is defined by [51]

$$E_{nl} = -R \frac{Z_c^2}{(n - \delta_l)^2}, \quad (1)$$

with Z_c the net charge state of the core ($Z_c = 4$ for Sn³⁺), and n the principal quantum number. R relates to the

Rydberg constant R_∞ as $R = R_\infty(1 + m_e/M)^{-1}$, with m_e and M the electronic and nuclear mass, respectively. Following the review by Edlén [51], the quantum defect can be written as a Taylor expansion in $1/n^{*2}$ with n^* being the apparent principal quantum number $n^* = n - \delta_l$, with quantum defect δ_l ,

$$\delta_l = a \left(\frac{1}{n^{*2}} \right) + b \left(\frac{1}{n^{*2}} \right)^2 + \dots \quad (2)$$

The quantum defect becomes smaller with increasing angular momentum. For high- n values the first term dominates and the minute change of δ_l as a function of $1/n^{*2}$ becomes linear. Additionally, it is well-established that a is positive for $l \leq l_{\text{core}}$, while a is negative for $l > l_{\text{core}}$ [51]. For Sn³⁺ with its 4d¹⁰ core, $l_{\text{core}} = 2$.

V. RESULTS AND DISCUSSION

Using the iterative guidance from the COWAN code as described above, we assign the newly found lines. The new Sn IV line assignments are summarized in Table II. The level energies of excited states are determined with respect to the 6s, which is used as an anchor level considering that transitions to the 5s ground state are outside our detection region. The optimization of level energies is performed using Kramida's code LOPT [53], and the final results are presented in Table III.

The consistency of the energies of levels within a specific l series is verified by determining the respective quantum defects. Quantum defects are calculated using Eq. (1) with the found level energies relative to the ionization limit. Therefore an accurate value of this limit is needed.

The ionization limit of 328 550 (300) cm⁻¹, tabulated in the NIST database [23], is based on the determination of the series limit of the ns levels ($n = 5 - 7$). Ryabtsev *et al.* [30] extended this ns series with 8s, 9s, and 10s. Using the extended ns series they were able to refine the ionization limit to 328 910 (5) cm⁻¹. The ionization limit can be further improved by taking additional levels into account. Configurations which are prone to shifting of the level energies by configuration interaction effects (np , nd , and nf , further described in Section V C) are however unsuitable for determining the series limit. Therefore we only use the ng , nh and ni configurations to refine the ionization limit. The results from analysis with the POLAR code [54] is 328 908.4 cm⁻¹ with a statistical error of 0.3 cm⁻¹. Combining this in quadrature with the uncertainty of 6s anchor level, we arrive at a total uncertainty of 2.1 cm⁻¹. Fig. 5 presents the quantum defects of the Sn IV levels as a function of $1/n^{*2}$. Overall, a smooth dependence is found for all angular quantum numbers from $l=0$ (s) up to $l=6$ (i), underpinning the consistency of our identifications.

For the discussion of details of the line assignments and energy levels we consider separately levels for which the

TABLE II. Assignments and vacuum wavelengths (in nm) of UV and visible transitions of SnIV identified in this work. The upper and lower energy levels indicating the transition represent the nl one-electron orbital outside the $[\text{Kr}]4d^{10}$ core configuration. The wavelengths determined in this work are averaged centroid positions of Gaussian fits in spectra taken at different laser energies. The intensity I represents the area-under-the-curve of this line in the 30 mJ spectrum. gA factors from the upper level result from analysis with the COWAN code. The fine structure for several high- l states could not be resolved experimentally, therefore no individual angular momenta are given and the reported gA is the summed value of the three possible transitions.

λ (nm)	I (arb.un.)	gA (10^8 s^{-1})	lower		upper	
			nl	J	nl	J
202.08	1	10.5	5f	7/2	8g	9/2
203.36	2	8.6	5f	5/2	8g	7/2
231.72	2	14.4	5g		8h	
242.55	3	0.3	6d	3/2	6f	5/2
245.15	1	0.5	6d	5/2	6f	7/2
273.75	3	2.2	7p	1/2	8d	3/2
279.91	8	3.8	7p	3/2	8d	5/2
287.82	48	30.4	5g		7h	
357.01	204	24.6	5f	7/2	6g	9/2
360.99	233	20.2	5f	5/2	6g	7/2
393.41	27	5.7	6f	7/2	8g	9/2
395.08	35	4.4	6f	5/2	8g	7/2
459.04	2 518	93.7	5g		6h	
463.49	202	15.1	6g		8h	
467.41	107	14.7	6h		8i	
504.82	90	2.0	7p	1/2	8s	1/2
529.12	40	3.5	7p	3/2	8s	1/2
541.12	366	7.9	7p	1/2	7d	3/2
563.38	662	12.4	7p	3/2	7d	5/2
563.60	60	0.7	5g	7/2	6f	5/2
567.00	42	0.9	5g	9/2	6f	7/2
569.13	68	1.3	7p	3/2	7d	3/2
575.85	881	10.0	6d	3/2	5f	5/2
589.40	71	6.9	6f	7/2	7g	9/2
593.13	368	5.3	6f	5/2	7g	7/2
597.93	940	12.5	6d	5/2	5f	7/2
643.43	154	3.3	5f	7/2	7d	5/2
664.32	103	2.3	5f	5/2	7d	3/2
673.51	36	0.5	6d	3/2	7p	3/2
688.89	212	3.8	6d	5/2	7p	3/2
717.44	98	1.8	6d	3/2	7p	1/2
759.65	316	49.6	6g		7h	
769.75	388	49.6	6h		7i	

valence electron does or does not penetrate the electronic core, i.e., levels with $l \leq l_{\text{core}}$ and $l > l_{\text{core}}$, respectively. For Sn^{3+} with its $4d^{10}$ core, $l_{\text{core}} = 2$. Anomalous effects on the fine structure splitting of the $5d$ and nf configura-

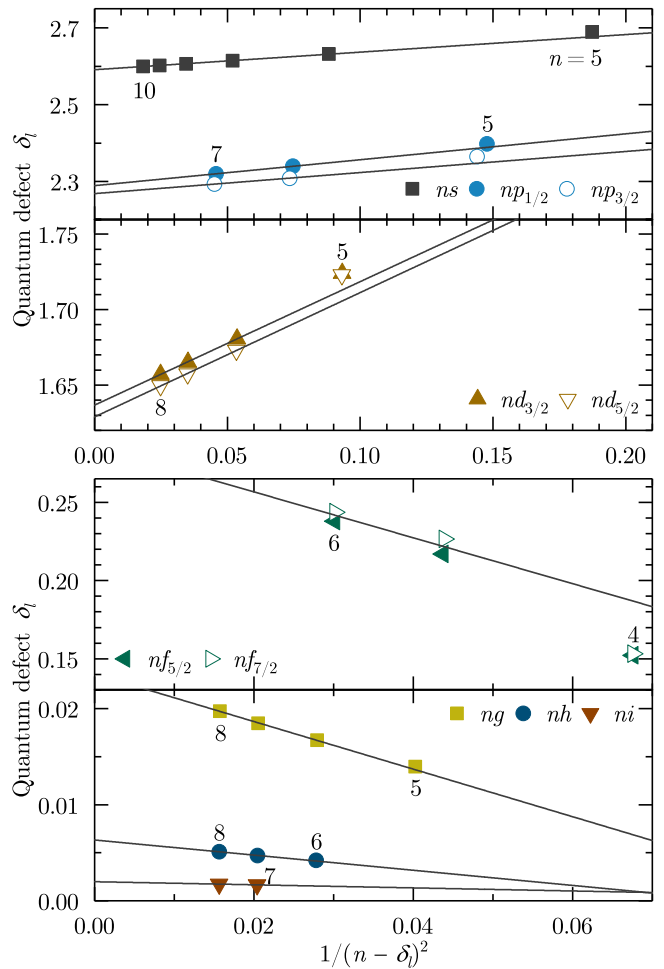


FIG. 5. Quantum defect values as a function of $1/n^{*2}$ of the SnIV energy levels, for $l \leq l_{\text{core}}$ (upper graph) and $l > l_{\text{core}}$ (lower graph). The quantum defects are calculated using Eq. (1) and the refined ionization limit of $328\,908.4 \text{ cm}^{-1}$. The black lines are linear fits of the data points where the lowest level is excluded (except for the ni configuration).

rations are discussed and explained separately. Finally, Fig. 6 depicts the extended level diagram of SnIV as a concise summary of our results.

A. $l \leq l_{\text{core}}$ configurations

The $5s$, $6s$, and $7s$ levels are included in Moore's tables [24]. The excitation energies of the $8s$, $9s$ and, $10s$ levels were determined in EUV spectroscopy experiments by Ryabtsev *et al.* [30] in which transitions to the $5p \ ^2P_{1/2,3/2}$ terms were measured. The $5p \ ^2P_{1/2,3/2}$ terms can be populated from the nd series, this nd series is known up $n = 7$. The highest known np configuration so far was $6p$. All transition in the optical spectral range (Table II) between both ns and nd and $6p$ agree with the literature excitation energies of the respective levels.

TABLE III. Energy levels of Sn^{3+} , with its ground state $[\text{Kr}]4d^{10}5s$. The experimental values obtained in this work are presented, next to the known values from literature given in Refs. [24, 30]. The experimental level energies of excited states are calculated with respect to the $6s$ anchor level and are the result from analysis with the LOPT code. The statistical uncertainty is presented in parentheses. The Total column contains the sum of FSCC calculations including Breit interaction and QED effects. As a comparison to theoretical values, relativistic many-body perturbation theory (RMBPT) calculations obtained from Ref. [40] are shown, while other known fine structure splittings are given in Table IV. The fine structure splitting of several high- nl levels are smaller than 0.5 cm^{-1} and not resolved experimentally. In those cases, a value of the angular momentum is omitted. The ionization potential (IP) is presented at the bottom of the Table.

nl	J	$E_{\text{experiment}} (\text{cm}^{-1})$		$E_{\text{theory}} (\text{cm}^{-1})$				RMBPT [40]
		this work	literature	FSCC	ΔE_{Breit}	ΔE_{QED}	Total	
5p	1/2		69 563.9 [24]	69 850	62	-171	69 741	69 265
	3/2		76 072.3 [24]	76 447	-26	-165	76 256	75 736
5d	3/2	165 304(1)	165 304.7 [24]	165 974	-123	-205	165 646	164 538
	5/2	165 409(1)	165 410.8 [24]	166 731	-145	-204	166 382	165 283
4d ⁹ 5s ²	5/2	169 233.6(8)	169 233.6 [24]					
	3/2		177 889.0 [24]					
6s	1/2	174 138.8(4)	174 138.8 [24]	174 478	-99	-143	174 236	
6p	1/2	197 850.6(6)	197 850.9 [24]	198 292	-74	-193	198 025	
	3/2	200 030.1(4)	200 030.8 [24]	200 512	-103	-193	200 216	
4f	7/2	210 258.2(6)	210 257.7 [24]	210 912	-158	-200	210 554	209 418
	5/2	210 317.9(7)	210 318.2 [24]	210 983	-156	-200	210 627	209 494
6d	3/2	234 797.0(1)	234 795.7 [24]	235 509	-134	-203	235 171	
	5/2	235 128.7(2)	235 127.7 [24]	235 842	-144	-201	235 497	
7s	1/2	237 617(1)	237 615.7 [24]	238 219	-123	-175	237 920	
7p	1/2	248 735.4(2)		249 402	-110	-197	249 094	
	3/2	249 644.8(1)		250 454	-124	-97	250 233	
5f	7/2	251 853.0(2)		252 984	-157	-201	252 626	250 981
	5/2	252 162.6(2)		253 023	-155	-202	252 666	251 025
5g	7/2	258 283.2(3)	258 282.3 [24]	258 782	-143	-201	258 439	256 868
	9/2	258 283.2(3)	258 282.7 [24]	258 782	-143	-201	258 439	256 872
7d	3/2	267 215.5(2)	267 247.6 [30]	267 815	-138	-202	267 475	
	5/2	267 394.7(2)	267 395.7 [30]	267 993	-143	-203	267 647	
8s	1/2	268 544.3(3)	268 544 [30]	269 193	-132	-166	268 895	
6f	7/2	275 919.8(3)		276 430	-153	-201	276 076	
	5/2	276 026.2(3)		276 450	-152	-201	276 097	
6g	9/2	279 863.6(2)		280 580	-143	-202	280 235	
	7/2	279 863.6(2)		280 581	-143	-201	280 237	
6h		280 067.8(7)						
8d	3/2	285 265(1)		285 834	-140	-197	285 497	
	5/2	285 370(1)		285 937	-143	-197	285 597	
9s	1/2		286 013 [30]					
7g		292 886.0(3)						
7h		293 027.6(3)						
7i		293 059.0(2)						
10s	1/2		296 844 [30]					
8g		301 338.2(6)						
8h		301 439.2(7)						
8i		301 462.3(7)						
IP		328 908.4(3)	328 550 [24]	329 343	-143	-201	328 999	327 453
			328 910 [30]					

TABLE IV. Comparison of fine structure splittings in np , nd , and nf configurations of Sn IV. Experimental values stem from either a direct comparison of $\Delta J = 0$ and $\Delta J = -1$ transitions or indirectly from the optimized level structure. The latter are labeled by an asterisk. The upper part of the Table contains results published in this work, the lower part shows results obtained from Refs. [24, 40–44].

	fine structure splitting (cm ⁻¹)									
	5 <i>p</i>	6 <i>p</i>	7 <i>p</i>	5 <i>d</i>	6 <i>d</i>	7 <i>d</i>	8 <i>d</i>	4 <i>f</i>	5 <i>f</i>	6 <i>f</i>
experiment		2 179.5	909.1	107.0	331.1	179.3	105.4*	-60.4	-309.6*	-106.4*
COWAN	6 417	2 237	911	170	240	130	79	34	-228	-73
FSCC	6 515	2 191	1 139	736	326	172	100	-73	-40	-21
CI+MBPT				162					-620	
experiment [24]	6 508.4	2 179.9		106.1	332.0			-60.5		
RMBPT [40]	6 471			745				-76	-44	
RPTMP ^a [41]								-60	-22	
MCDHF [42]								-71		
FCV [43]								-85		
RHF ^a [44]	5 960			641				-108	-72	

^a Fine structure splittings deduced from transition wavelengths.

non-relativistic electron repulsion and the frequency independent Breit operator,

$$B_{ij} = -\frac{1}{2r_{ij}}[\boldsymbol{\alpha}_i \cdot \boldsymbol{\alpha}_j + (\boldsymbol{\alpha}_i \cdot \mathbf{r}_{ij})(\boldsymbol{\alpha}_j \cdot \mathbf{r}_{ij})/r_{ij}^2], \quad (5)$$

and is correct to second order in the fine structure constant α .

The calculations of the transition energies of Sn³⁺ start from the closed-shell reference [Kr]4*d*¹⁰ configuration of Sn⁴⁺. After the first stage of the calculation, consisting of solving the relativistic Hartree-Fock equations and correlating the closed-shell reference state, a single electron was added to reach the desired Sn³⁺ state. A large model space was used in this calculation, comprising 10 *s*, 8 *p*, 6 *d*, 6 *f*, 4 *g*, 3 *h*, and 2 *i* orbitals in order to obtain a large number of excitation energies and to reach optimal accuracy. The intermediate Hamiltonian method was employed to facilitate convergence [57].

The uncontracted universal basis set [58] was used, consisting of even-tempered Gaussian type orbitals, with exponents given by

$$\xi_n = \gamma \delta^{(n-1)}, \quad \gamma = 106\,111\,395.371\,615, \quad (6)$$

$$\delta = 0.486\,752\,256\,286.$$

The basis set was composed of 37 *s*, 31 *p*, 26 *d*, 21 *f*, 16 *g*, 11 *h*, and 6 *i* functions; the convergence of the obtained transition energies with respect to the size of the basis set was verified. All the electrons were correlated.

The FSCC calculations were performed using the Tel-Aviv Relativistic Atomic FSCC code (TRAFS-3C) [59]. To account for the QED corrections to the transition energies we applied the model Lamb shift operator (MLSO) of Shabaev and co-workers [60] to the atomic no-virtual-pair many-body DCB Hamiltonian as implemented into the QEDMOD program. Our implementation of the MLSO

formalism into the Tel Aviv atomic computational package allows us to obtain the vacuum polarization and self-energy contributions beyond the usual mean-field level, namely at the DCB-FSCCSD level.

The FSCC results are compared to the experimental level energies and several results of previous theoretical work in Table III and are overall in good agreement. Typical differences with experiment are about 100 to 300 cm⁻¹ which is on the 10⁻³ level of the calculated excitation energies. Concerning the measured anomalous fine structure intervals of the 5*d* ²D and 5*f*, 6*f* ²F terms, presented in Table IV, the apparent narrowing of the fine-structure interval of the 5*d* ²D term and the widening of the 5*f*, 6*f* ²F term intervals are not reproduced by the FSCC calculations. The FSCC intervals are similar to those presented in earlier theoretical investigations [40–44].

For the 5*d* ²D term the fine structure interval is measured at 107 cm⁻¹, while all theoretical results are higher by a factor of approximately seven, see Table IV. When inspecting the level diagram (Fig. 6) one notices that the 5*d* ²D term might suffer from configuration interaction of the doubly-excited 4*d*⁹ 5*s*² levels.

To quantify the strength of the configuration interaction we employ configuration interaction many-body perturbation theory (CI+MBPT) calculations using the AMBiT code. Details of the AMBiT code can be found in Refs. [61–64]. To begin our discussion of the AMBiT treatment of the problem, first consider the 5*d* ²D_{5/2} and 4*d*⁹ 5*s*² ²D_{5/2} levels as a two-level system. In the absence of interaction between them, they have theoretical energies ϵ_1 and ϵ_2 , respectively. ϵ_1 is, to a good approximation, the FSCC value of the 5*d* ²D_{5/2} level, since in that calculation the one-hole two-particle 4*d*⁹ 5*s*² ²D_{5/2} level is not explicitly included. If we now add an interaction V , then the states mix and the levels repel each other.

The Hamiltonian of this two-level system is

$$H = \begin{pmatrix} \epsilon_1 & V \\ V & \epsilon_2 \end{pmatrix}.$$

Writing $\Delta\epsilon = \epsilon_2 - \epsilon_1 > 0$, the $5d^2D_{5/2}$ level shifts down by an amount

$$\delta = \frac{\Delta E - \Delta\epsilon}{2} = \frac{\Delta\epsilon}{2} \left(\sqrt{1 + \frac{4V^2}{\Delta\epsilon^2}} - 1 \right) = b^2 \Delta E, \quad (7)$$

where $\Delta E = E_2 - E_1$ is the difference between the eigenvalues of H and b is the smaller component of the normalized eigenvector $(a, b)^T$.

Using AMBiT, we calculate theoretical values for the parameters ΔE_{th} and b , from which we can obtain the interaction $V = -ab\Delta E_{\text{th}}$. However, the values of ΔE_{th} and b are sensitive to details of the calculations. In particular, it is challenging to match theoretical with experimental level energies at a good level of accuracy. On the other hand, the values of V that we obtain are highly stable since they are not sensitive to the separation. If we use the experimental separation $\Delta E_{\text{exp}} = 3823 \text{ cm}^{-1}$ and $|V| = 1523 \text{ cm}^{-1}$ from AMBiT, we find the energy shift of the $5d^2D_{5/2}$ level due to interaction with the hole state,

$$\delta = \frac{\Delta E_{\text{exp}}}{2} \left(1 - \sqrt{1 - \frac{4V^2}{\Delta E_{\text{exp}}^2}} \right), \quad (8)$$

yielding -755 cm^{-1} . The $5d^2D_{3/2}$ level also shifts down due to interaction with the $4d^9 5s^2 2D_{3/2}$ hole level. However, the energy difference is three times larger, and since $b \sim 1/\Delta E$, the energy shift is smaller by approximately a factor of three. We calculate $|V| = 1498 \text{ cm}^{-1}$ for this pair of levels, so Eq. (8) gives a level shift of -181 cm^{-1} . The change in the $5d$ fine-structure splitting is therefore -574 cm^{-1} which is close to the difference between experiment and FSCC calculation of -629 cm^{-1} .

In support of the role of configuration interaction on the $5d^2D$ fine structure, FSCC calculations were performed for isoelectronic In^{2+} ions in which there is a much larger energy difference between the $5d^2D$ term and the doubly-excited $4d^9 5s^2 2D_{5/2}$ level [24]. Thus a better agreement with FSCC calculations is expected. In comparison to Sn^{3+} , for In^{2+} the difference between experiment [24] and FSCC indeed reduces strongly from a factor of seven to only 30% (298 versus 398 cm^{-1}).

Before discussing the impact of configuration interaction on the fine structure of the $5f^2F$ and $6f^2F$ terms we note that the $4f^2F$ exhibits an inverted fine structure with the $J = 7/2$ level being more strongly bound than the $J = 5/2$ level by approximately 60 cm^{-1} . The occurrence of this inversion of the fine structure and the actual value of the fine-structure interval results from an intricate balance between relativistic, spin-orbit and core polarization effects and has been the subject of a variety of theoretical approaches calculating the $4f^2F$

fine-structure along the isoelectronic sequence of Ag-like ions [40–44].

We confirm the fine structure of the $4f^2F$ term by measuring the wavelengths of the transitions from the $5g^2G$ levels and the transitions to the $5d^2D$ levels. Weaker transitions from the $6d^2D$ term to the doubly-excited $4d^9 5s^2 2D_{5/2}$ level are observed additionally. A comparison of the fine structure splitting of the observed nf^2F levels with theoretical calculations is given in Table IV. Both measurements and theoretical calculations agree on an inverted fine structure splitting for these nf^2F terms. However the magnitude of the fine structure splitting of the $5f$ and $6f$ terms are much smaller than our experimental ones.

In similar fashion to the $5d^2D$ levels, the $5f^2F$ fine-structure splitting is strongly affected by interaction with hole states. However, the $5f^2F$ case is more complicated because the $4d^9 5s 5p$ configuration has seven configuration state functions (CSFs) with $J = 5/2$ and four CSFs with $J = 7/2$. The CSFs tend to be strongly mixed with each other, and also have small contributions of CSFs belonging to other configurations. Therefore, rather than treat the system as a few-level system, we use the approach of perturbation theory.

Using AMBiT we obtain energies for the $4d^9 5s 5p$ levels as well as a mixing coefficient. At first order in perturbation theory, the coefficient of ψ_{5f} in the level ψ_i is simply

$$b_{5f} = \frac{V_{i,5f}}{E_i - E_{5f}}.$$

From our AMBiT values of b_{5f} and E_i , we extract values for the matrix element $V_{i,5f}$. Again these are relatively stable for different calculations, even though the energies and b coefficients can change dramatically.

The corresponding energy shift of the $5f$ level is $\delta_{5f} = V_{i,5f}^2 / \Delta E_{\text{exp}}$. Unfortunately we do not have precise experimental determinations of most of the interaction $4d^9 5s 5p$ levels. Instead we use the results of COWAN calculations (Ref. [30]) to obtain an approximation to the level shifts. The results are presented in Table V.

We see that while each of the $5f$ levels are shifted by interactions with the hole levels, the change in the fine-structure splitting is dominated by the interaction of the $5f^2F_{7/2}$ level with a hole state at 260398 cm^{-1} . The final expected shift is 580 cm^{-1} , overestimating the actual difference between experimental fine-structure and FSCC calculations of 270 cm^{-1} . Nevertheless, given the uncertainties in our estimation of V and the location of the doubly-excited levels, we arrive at a plausible explanation for the observed anomaly.

A similar explanation can be given for the observed difference in fine structure splitting for the $6f^2F$ term, interacting with the high-lying levels in the same series of hole states. Because the energy differences between these levels are larger, this effect may reasonably be expected to be smaller than for the $5f^2F$ levels. Likewise, the $7p^2P$ is expected to interact with several doubly-excited levels.

TABLE V. Sn IV $4d^9 5s 5p$ level energies as candidates for possible configuration interaction with the nf levels. The level energies are obtained from COWAN code calculations published in Ref. [30]. The matrix elements $|V_{i,5f}|$ are calculated using the AMBiT code. The resulting shift of the $5f$ level by configuration interaction by the level is given by δ_{5f} . The $J = 5/2$ levels interact with the $5f \ ^2F_{5/2}$, similarly the $J = 7/2$ levels with $5f \ ^2F_{7/2}$.

E_i (cm $^{-1}$) [30]	J	$ V_{i,5f} $	δ_{5f}
226 363	5/2	3	0
231 318	5/2	484	11
239 582	5/2	765	47
242 203	5/2	622	39
249 541	5/2	41	1
263 718	5/2	111	-1
269 440	5/2	1341	-104
231 090	7/2	72	0
239 920	7/2	417	15
246 851	7/2	601	72
260 398	7/2	2404	-676

We also performed COWAN calculations to investigate the terms described above. The number of fitted parameters in this case is reduced by tying the Hartree-Fock ratios to the spin-orbit parameters for the np , nd , and nf levels. The $4d^9 5s 5p$ levels are taken from Ref. [30] (included in Table V). The two $4d^9 5s^2 \ ^2D$ levels were calculated with two adjustable parameters. All interaction parameters were fixed at 0.8 of their Hartree-Fock values. The number of levels determined was insufficient to more accurately fit the parameters. Results of the calcu-

lation are included in Table IV and show good agreement with the experimental results, although the inversion of the $4f \ ^2F$ level is not reproduced. The agreement for all other nf and the np and nd levels underlines the significant role of configuration interaction in a quasi-one-electron system like Sn $^{3+}$.

VI. CONCLUSION

Optical techniques are useful diagnostics in plasma sources of EUV light in nanolithography. We present the ultraviolet and optical spectra of a laser-produced tin plasma. The lines belonging to Sn $^{3+}$ are identified using a convenient masking technique. The 33 newly found lines are used to determine 13 new configurations with iterative guidance from COWAN code calculations. The level energies are verified using quantum-defect scaling procedure, leading to the refinement of the ionization limit to 328 908.4 cm $^{-1}$ with an uncertainty of 2.1 cm $^{-1}$. FSCC calculations are generally in good agreement with present measurements. The anomalous behavior of the $5d \ ^2D$ and $nf \ ^2D$ terms is shown to arise from configuration interaction with doubly-excited levels by joining the strengths of FSCC, COWAN and CI+MBPT approaches.

ACKNOWLEDGMENTS

Part of this work has been carried out at the Advanced Research Center for Nanolithography, a public-private partnership between the University of Amsterdam, the Vrije Universiteit Amsterdam, the Netherlands Organization for Scientific Research (NWO), and the semiconductor equipment manufacturer ASML.

-
- [1] V. Y. Banine, K. N. Koshelev, and G. H. P. M. Swinkels, *J. Phys. D* **44**, 253001 (2011).
 - [2] W. Svendsen and G. O'Sullivan, *Phys. Rev. A* **50**, 3710 (1994).
 - [3] J. W. Coenen, G. De Temmerman, G. Federici, V. Philipps, G. Sergienko, G. Strohmayer, A. Terra, B. Unterberg, T. Wegener, and D. C. M. van den Bekerom, *Phys. Scripta* **2014**, 014037 (2014).
 - [4] G. G. van Eden, T. W. Morgan, D. U. B. Aussems, M. A. van den Berg, K. Bystrov, and M. C. M. van de Sanden, *Phys. Rev. Lett.* **116**, 135002 (2016).
 - [5] G. G. Eden, V. Kvon, M. C. M. van de Sanden, and T. W. Morgan, *Nat. Commun.* **8**, 192 (2017).
 - [6] M. S. Mason and G. Eng, *J. Vac. Sci. Technol. A* **25**, 1562 (2007).
 - [7] L. M. Hobbs, D. E. Welty, D. C. Morton, L. Spitzer, and D. G. York, *Astrophys. J.* **411**, 750 (1993).
 - [8] C. R. Proffitt, C. J. Sansonetti, and J. Reader, *Astrophys. J.* **557**, 320 (2001).
 - [9] P. Chayer, S. Vennes, J. Dupuis, and J. W. Kruk, *Astrophys. J. Lett.* **630**, L169 (2005).
 - [10] S. J. Adelman, W. P. Bidelman, and D. M. Pyper, *Astrophys. J. Suppl. Ser.* **40**, 371 (1979).
 - [11] B. D. Savage and K. R. Sembach, *Annu. Rev. Astron. Astrophys.* **34**, 279 (1996).
 - [12] U. J. Sofia, D. M. Meyer, and J. A. Cardelli, *Astrophys. J. Lett.* **522**, L137 (1999).
 - [13] I. de Andrés-García, A. Alonso-Medina, and C. Colón, *Mon. Not. R. Astron. Soc.* **455**, 1145 (2016).
 - [14] M. S. Dimitrijević, Z. Simić, R. Stamm, J. Rosato, N. Milovanović, and C. Yubero, *Atoms* **6**, 10 (2018).
 - [15] S. Biswas, A. Das, A. Bhowmik, and S. Majumder, *Mon. Not. R. Astron. Soc.* **477**, 5605 (2018).
 - [16] A. Roy, S. S. Harilal, S. M. Hassan, A. Endo, T. Mocek, and A. Hassanein, *Laser Part. Beams* **33**, 175 (2015).
 - [17] R. W. Coons, S. S. Harilal, D. Campos, and A. Hassanein, *J. Appl. Phys.* **108**, 063306 (2010).
 - [18] S. S. Harilal, B. O'Shay, M. S. Tillack, and M. V. Mathew, *J. Appl. Phys.* **98**, 013306 (2005).
 - [19] H. Lan, H. Lei, D. Zuo, X. Wang, and G. Zheng, *Vacuum* **135**, 86 (2017).

- [20] J. Iqbal, R. Ahmed, M. Rafique, M. Anwar-ul Haq, and M. A. Baig, *Laser Phys.* **26**, 076001 (2016).
- [21] S. Namba, S. Fujioka, H. Sakaguchi, H. Nishimura, Y. Yasuda, K. Nagai, N. Miyanaga, Y. Izawa, K. Mima, K. Sato, *et al.*, *J. Appl. Phys.* **104**, 013305 (2008).
- [22] E. R. Kieft, J. J. A. M. van der Mullen, G. M. W. Kroesen, V. Banine, and K. N. Koshelev, *Phys. Rev. E* **70**, 066402 (2004).
- [23] A. Kramida, Yu. Ralchenko, J. Reader, and NIST ASD Team, NIST Atomic Spectra Database (ver. 5.5.6), [Online]. Available: <https://physics.nist.gov/asd> [2018, July 7]. National Institute of Standards and Technology, Gaithersburg, MD. (2018).
- [24] C. Moore, *Atomic Energy Levels*, Vol. III (Nat. Bur. Stand., 1958).
- [25] J. Reader, C. H. Corliss, W. L. Wiese, and G. A. Martin, *NSRDS-NBS* **68** (1980).
- [26] J. A. Carroll, *Phil. Trans. R. Soc. A* **225**, 357 (1926).
- [27] K. R. Rao, *Proc. Phys. Soc.* **39**, 408 (1926).
- [28] R. C. Gibbs, A. M. Vieweg, and C. W. Gartlein, *Phys. Rev.* **34**, 406 (1929).
- [29] R. J. Lang, *Phys. Rev.* **35**, 445 (1930).
- [30] A. N. Ryabtsev, S. S. Churilov, and É. Y. Kononov, *Opt. Spectr.(USSR)(English Transl.)* **100**, 652 (2006).
- [31] C.-M. Wu, *Atomic spark spectra of tin, Sn III, Sn IV, Sn V*, Master's thesis, University of British Columbia (1967).
- [32] E. H. Pinnington, J. A. Kernahan, and W. Ansbacher, *Can. J. Phys.* **65**, 7 (1987).
- [33] J. A. Kernahan, E. H. Pinnington, W. Ansbacher, and J. L. Bahr, *Nucl. Instr. Meth. Phys. Res. B* **9**, 616 (1985).
- [34] T. Andersen, A. K. Nielsen, and G. Sørensen, *Phys. Scripta* **6**, 122 (1972).
- [35] V. Kaufman, J. Sugar, T. A. M. Van Kleef, and Y. Joshi, *J. Opt. Soc. Am. A* **2**, 426 (1985).
- [36] P. Dunne and G. O'Sullivan, *J. Phys. B* **25**, L593 (1992).
- [37] A. N. Ryabtsev, S. S. Churilov, and É. Y. Kononov, *Opt. Spectr.(USSR)(English Transl.)* **102**, 354 (2007).
- [38] M. A. Lysaght, D. Kilbane, A. Cummings, N. Murphy, P. Dunne, P. van Kampen, J. T. Costello, and E. T. Kennedy, *J. Phys. B* **38**, 4247 (2005).
- [39] M. Lysaght, D. Kilbane, N. Murphy, A. Cummings, P. Dunne, and G. O'Sullivan, *Phys. Rev. A* **72**, 014502 (2005).
- [40] U. I. Safronova, I. M. Savukov, M. S. Safronova, and W. R. Johnson, *Phys. Rev. A* **68**, 062505 (2003).
- [41] E. P. Ivanova, *At. Data Nucl. Data Tables* **97**, 1 (2011).
- [42] X.-B. Ding, F. Koike, I. Murakami, D. Kato, H. A. Sakaue, C.-Z. Dong, and N. Nakamura, *J. Phys. B* **45**, 035003 (2012).
- [43] J. Grumer, R. Zhao, T. Brage, W. Li, S. Hultdt, R. Hutton, and Y. Zou, *Phys. Rev. A* **89**, 062511 (2014).
- [44] K.-T. Cheng and Y.-K. Kim, *J. Opt. Soc. Am.* **69**, 125 (1979).
- [45] D. Kurilovich, A. L. Klein, F. Torretti, A. Lassise, R. Hoekstra, W. Ubachs, H. Gelderblom, and O. O. Versolato, *Phys. Rev. Applied* **6**, 014018 (2016).
- [46] W. F. Meggers, *J. Res. Nat. Bur. Stand.* **24**, 153 (1940).
- [47] K. Haris, A. Kramida, and A. Tauheed, *Phys. Scripta* **89**, 115403 (2014).
- [48] K. Haris and A. Tauheed, *Phys. Scripta* **85**, 055301 (2012).
- [49] T. A. M. Van Kleef and Y. N. Joshi, *Phys. Scripta* **24**, 557 (1981).
- [50] A. N. Ryabtsev, S. S. Churilov, and E. Y. Kononov, *Phys. Scripta* **72**, 377 (2005).
- [51] B. Edlén, in *Spektroskopie I (Handbuch der Physik)* (Springer, 1964) pp. 80–220.
- [52] R. D. Cowan, *The Theory of Atomic Structure and Spectra* (University of California Press, 1981) modified by A. Kramida.
- [53] A. Kramida, *Comput. Phys. Commun.* **182**, 419 (2011).
- [54] C. J. Sansonetti, "Fortran computer code POLAR," private communication (2005).
- [55] J. Sucher, *Phys. Rev. A* **22**, 348 (1980).
- [56] Y. Ishikawa, R. Baretty, and R. C. Binning Jr, *Chem. Phys. Lett.* **121**, 130 (1985).
- [57] E. Eliav, M. J. Vilkas, Y. Ishikawa, and U. Kaldor, *J. Chem. Phys.* **122**, 224113 (2005).
- [58] G. L. Malli, A. B. F. Da Silva, and Y. Ishikawa, *Phys. Rev. A* **47**, 143 (1993).
- [59] TRAFS-3C code (Tel-Aviv Relativistic Atomic Fock-Space coupled cluster code), written by E. Eliav, U. Kaldor and Y. Ishikawa (1990-2013), with contributions by A. Landau.
- [60] V. M. Shabaev, I. I. Tupitsyn, and V. A. Yerokhin, *Comput. Phys. Commun.* **189**, 175 (2015).
- [61] J. C. Berengut, V. V. Flambaum, and M. G. Kozlov, *Phys. Rev. A* **73**, 012504 (2006).
- [62] J. C. Berengut, *Phys. Rev. A* **84**, 052520 (2011).
- [63] J. C. Berengut, *Phys. Rev. A* **94**, 012502 (2016).
- [64] E. Kahl and J. C. Berengut, (2018), <https://arxiv.org/abs/1805.11265>.